PAPER

Equilibrium and non-equilibrium free carrier dynamics in 2D $Ti_3C_2T_x$ MXenes: THz spectroscopy study

To cite this article: Guangjiang Li *et al* 2018 *2D Mater.* **5** 035043

2D Materials

PAPER

RECEIVED
3 April 2018

REVISED
25 May 2018

ACCEPTED FOR PUBLICATION
11 June 2018

PUBLISHED
27 June 2018

Equilibrium and non-equilibrium free carrier dynamics in 2D $Ti_3C_2T_x$ MXenes: THz spectroscopy study

Guangjiang Li[1], Kateryna Kushnir[1], Yongchang Dong[2], Sergii Chertopalov[3], Apparao M Rao[2], Vadym N Mochalin[3,4], Ramakrishna Podila[2] and Lyubov V Titova[1]

[1] Department of Physics, Worcester Polytechnic Institute, Worcester, MA 01609, United States of America
[2] Department of Physics and Astronomy and Clemson Nanomaterials Institute, Clemson University, Clemson, SC 29634, United States of America
[3] Department of Chemistry, Missouri University of Science and Technology, Rolla, MO, United States of America
[4] Department of Materials Science and Engineering, Missouri University of Science and Technology, Rolla, MO, United States of America

E-mail: mochalinv@mst.edu, rpodila@g.clemson.edu and ltitova@wpi.edu

Keywords: MXene, THz spectroscopy, terahertz, carrier dynamics

Abstract

MXenes is an emerging class of 2D transition metal carbides, nitrides and carbonitrides which exhibit large conductivity, ultrahigh volumetric capacitance, high threshold for light-induced damage and nonlinear optical transmittance, making them attractive candidates for a variety of optoelectronic and electrochemical applications. Here, we report on equilibrium and non-equilibrium free carrier dynamics of $Ti_3C_2T_x$ gleaned from THz spectroscopic studies for the first time. $Ti_3C_2T_x$ showed high ($\sim 2 \times 10^{21}$ cm^{-3}) intrinsic charge carrier density and relatively high (~ 34 cm^2 V^{-1} s^{-1}) mobility of carriers with an exceptionally large, $\sim 46\,000$ cm^{-1} absorption in the THz range, which suggests that $Ti_3C_2T_x$ is well suited for THz detection. We also demonstrate that $Ti_3C_2T_x$ conductivity and THz transmission can be manipulated by photoexcitation, as absorption of near-infrared, 800 nm pulses is found to cause transient suppression of the conductivity that recovers over hundreds of picoseconds. The possibility of control over THz transmission and conductivity by photoexcitation suggests the promise for application of $Ti_3C_2T_x$ Mxenes in THz modulation devices and variable electromagnetic shielding.

1. Introduction

The recent emergence of two-dimensional (2D) materials facilitated the realization of novel optoelectronic and nanophotonic applications. In addition to extraordinary and strongly anisotropic electronic properties, many 2D materials exhibit strong light–matter interactions despite their atomic thickness [1–10]. Others and we recently demonstrated that an emerging class of 2D early transition metal carbides and carbonitride, MXenes, are ideal for femtosecond mode locking and optical isolation applications due to their high, $\approx$70 mJ cm^{-2} threshold for light-induced damage with up to 50% modulation depth [7, 11]. MXenes are a large family of 2D early transition metal carbides and nitrides with the chemical formula $M_{n+1}X_nT_x$ ($n = 1$–3), where M is an early transition metal, X is a carbon and/or nitrogen, and T_x represents surface termination groups such as =O, –OH, –F, etc [12–20]. Dangling bonds on MXene surfaces formed during synthesis are naturally passivated due to interactions with the environment, which allows for easy integration with photonic structures such as waveguides and cavities [10]. In addition to potenial photonic applications, layered 2D titanium carbides are actively researched as novel precious-metal-free conductive materials for electrochemical energy storage, with demonstrated ultrahigh volumetric capacitance up to 900 F cm^{-3} [13], transparent conductive electrodes and efficient photothermal convertors [14, 15]. Recent studies have demonstrated that efficiency of light-to-heat conversion in MXenes including $Ti_3C_2T_x$ can reach 100%, suggesting their applications in photothermal solar energy conversion devices as well as in novel photothermal tumor ablation approaches in oncology [21]. High electrical conductivity of $Ti_3C_2T_x$ results in a strong absorption across the microwave and terahertz (THz) range and makes it a promising new material for electromagnetic shielding [22, 23].

Combined with thermoelectric properties of $Ti_3C_2T_x$ MXenes, rivaling those of carbon nanotube films, large THz absorption also suggests potential application in THz detectors [10, 24]. Considering a wide range of potential photonic, electronic and electrochemical applications of MXenes, it is timely to address exisiting knowledge gaps to elucidate intrinsic carrier zero-field mobility in $Ti_3C_2T_x$ and understand the effects of photoexcitation on conductivity and ultrafast nonequilibrium dynamics of charge carriers.

Here, we used terahertz (THz) spectroscopy to study both equilibrium and non-equilibrium free carrier dynamics in a 16 nm thick $Ti_3C_2T_x$ MXene film. Picosecond-duration THz pulses with the bandwidth of 0.25–2 THz, or 1–10 meV, are uniquely suited for probing microscopic conductivity and free carrier dynamics [25, 26]. We report native frequency-dependent complex THz sheet conductivity, as well as the impact of photoexcitation with near-IR, 800 nm pulses on sheet conductivity and carrier mobility. We find that the mobility of intrinsic carriers within the individual metallic $Ti_3C_2T_x$ nanoplatelets is ~80 $cm^2 V^{-1} s^{-1}$. Long-range mobility within the film appears to be strongly suppressed by grain boundaries. We observe that photoexcitation with 800 nm pulses results in a transient suppression of conductivity that persists for hundreds of picoseconds. Like in graphene and other metallic systems, photoexcitation raises the temperature of the entire free carrier population, which then cools by emission of phonons and increasing the lattice temperature. Increased lattice temperature manifests in enhanced carrier scattering rate which leads to a suppressed conductivity. The conductivity recovers as the lattice cools by transfering heat both to the glass substrate underneath (vertically) and to the unexcited nanoplatelets within the sample (laterally). This process lasts significantly longer in $Ti_3C_2T_x$ film than in metallic graphene, lasting for hundreds of picoseconds compared to picoseconds time scale in graphene due to inherently lower thermal conductivity in a film composed of $Ti_3C_2T_x$ nanoplatelets with ~1 μm lateral dimensions.

2. Experimental methods

2.1. Fabrication of $Ti_3C_2T_x$ film

$Ti_3C_2T_x$ was synthesized by selective etching of aluminum atomic layers in Ti_3AlC_2 by MILD etching method described previously [13, 16, 17]. To synthesize $Ti_3C_2T_x$, 1 g of lithium fluoride (LiF) was added to 20 ml of 6 M hydrochloric acid (HCl) while stirring with a Teflon magnetic stir bar. Over the course of a few minutes, 1 g of Ti_3AlC_2 was added to the LiF/HCl mixture and the reaction proceeded for 24 h at 35 °C. After etching, the mixture was repeatedly washed with deionized water by centrifugation at 3500 rpm for 3 min and decantation of the acidic supernatant until a supernatant was obtained with a pH ~ 6. The supernatant was decanted, deionized water was added to the sediment, and the mixture was subjected to manual shaking for 5 min to delaminate the $Ti_3C_2T_x$ flakes, where T_x denotes mixed –OH, –O and –F terminations. The solution was centrifuged for 1 h at 3500 rpm and the supernatant was used for fabrication of $Ti_3C_2T_x$ films by the interfacial thin film technique described in our previous work [7]. Representative atomic force microscopy (AFM) images of the film studied here (figure 1(a)–(c)) show that it consists of crystalline platelets of the average height ~16 nm and lateral dimensions ~1 μm. As described in detail in our previous work [7], scanning electron microscopy, x-ray diffraction and AFM showed that individual $Ti_3C_2T_x$ laying in horizontal orientation and touching or overlapping one another result in a near uniform coverage of the substrate. No extended stacking in vertical direction was observed in SEM or XRD measurements [7]. Optical transmittance of the film is shown in figure 1(d). Despite the small thickness, the film is highly absorptive, with ~15% of incident light around 800 nm being absorbed.

2.2. THz spectroscopy

We investigated native conductivity of the $Ti_3C_2T_x$ film using THz time-domain spectroscopy in the transmission configuration [25, 27, 28]. THz probe pulses were generated by optical rectification of 100 fs, 800 nm pulses in 1 mm thick [1 1 0] ZnTe crystal. A combination of three off-axis parabolic mirrors collimated and focused the emitted THz pulses into a ~1.5 mm spot. The sample was placed behind the 1.5 mm aperture in the center of the THz spot. At normal incidence, THz pulse probes conductivity in the basal plane of $Ti_3C_2T_x$ film. Transmitted THz pulses were detected using free-space electrooptic sampling in the second 1 mm thick [1 1 0] ZnTe crystal. Coherent detection of the amplitude and phase of THz probe pulses in the time domain allows extracting the frequency-dependent complex conductivity of the sample by comparing the THz pulses transmitted through the substrate alone and the sample on the substrate. We have also examined the effect of photoexcitation on conductivity and carrier dynamics using optical pump—THz probe measurements [25, 29–32]. The sample was excited by 100 fs duration, 800 nm pulses. Optical pump beam was focused to ~5 mm spot at the sample location, ensuring that the probe THz pulse interrogates optically-induced changes in the uniformly photoexcited portion of the MXene film.

3. Results and discussion

3.1. THz time-domain spectroscopy: native conductivity

THz time domain spectroscopy is a non-contact probe of conductivity, as absorption of THz radiation is directly related to how conductive material is. Figure 2(a) shows THz pulses transmitted through

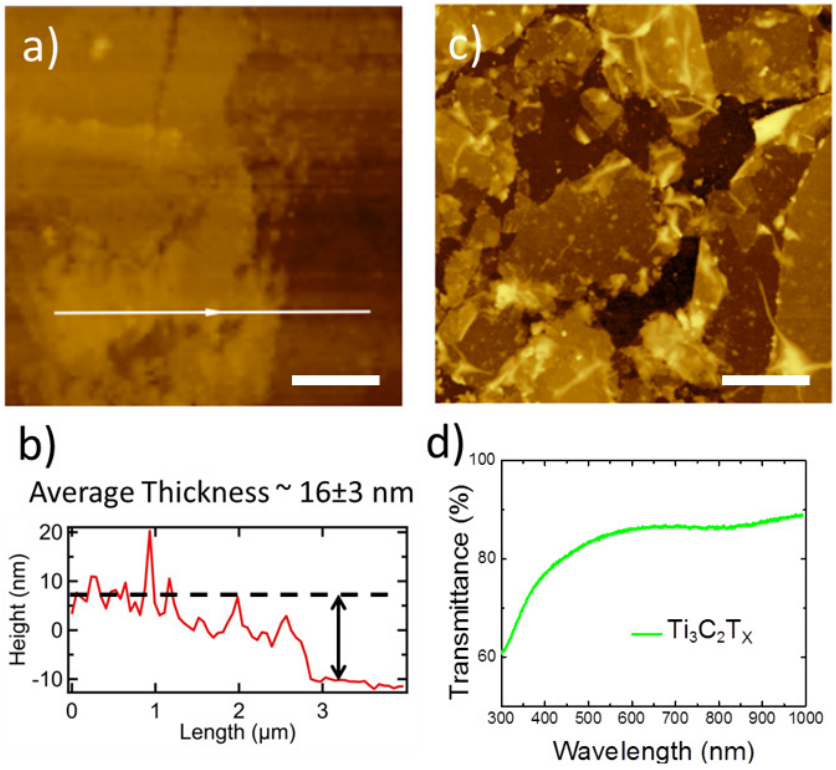

Figure 1. AFM characterization of $Ti_3C_2T_x$ films on glass substrates: individual nanoplatelets are ~16 nm thick (a) and (b) and have lateral dimensions of 1 μm (d). UV–VIS spectroscopy: film transmittance at 800 nm is ~85% (d). Scale bars in (a) and (c) are 1 μm.

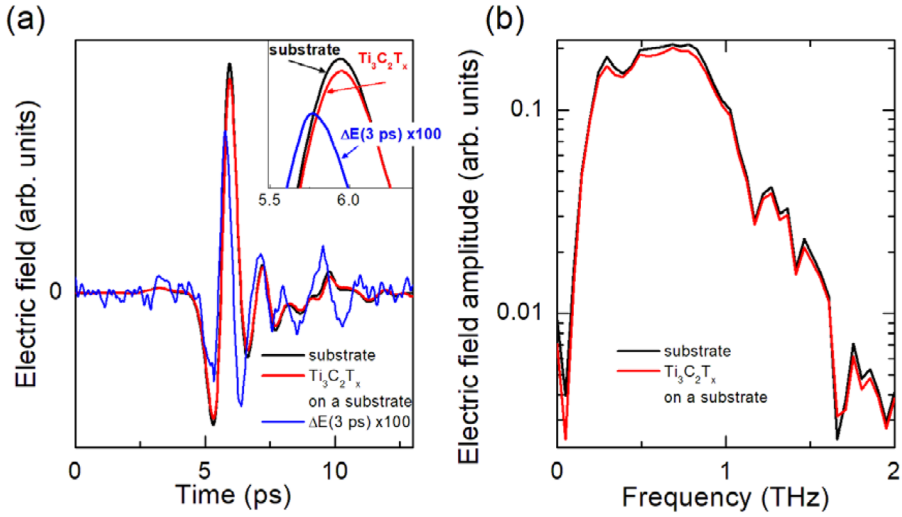

Figure 2. THz waveforms transmitted through the glass substrate (black curve) and through the $Ti_3C_2T_x$ film on the substrate (red). Photoinduced change in THz waveform transmission 3 ps after photoexcitation with 280 μJ cm^{-2}, 800 nm, multiplied by 100 for clarity, is shown in blue. Inset shows expanded view of the same waveforms.

a glass substrate alone (black curve) and through a ~16 nm thick $Ti_3C_2T_x$ film on a glass substrate. It also shows the change in transmission through the $Ti_3C_2T_x$ film induced by the photoexcitation, which will be discussed later. The corresponding Fourier transform amplitude spectra of the pulses transmitted through the substrate alone and the sample on a substrate are shown in figure 2(b). Assuming that the absorption in the film is responsible for the observed attenuation of the transmitted THz radiation which is estimated to be ~7.7% at the peak of THz waveform, we calculate the average absorption coefficient for stacked $Ti_3C_2T_x$ in the 02. −2.0 THz range to be ~46 000 cm^{-1}, in excellent agreement with theoretically predicted 45 000–60 000 cm^{-1} range, and smaller but comparable to the theoretically prediced THz absorption of stacked graphene flakes (60 000–80 000 cm^{-1}) [24]. Complex conductivity of the sample in the frequency domain ($\tilde{\sigma}(\omega)$) can be calculated using a thin film approximation from the amplitude (figure 2(a) and

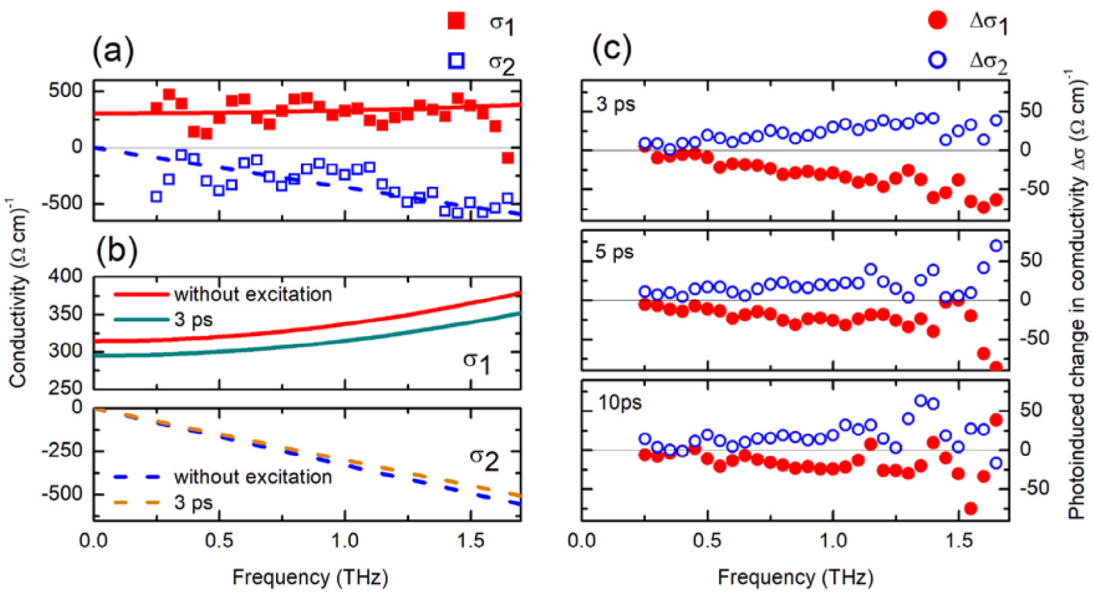

Figure 3. (a) Complex THz conductivity of the 16 nm $Ti_3C_2T_x$ film. Symbols represent experimental data extracted from THz waveforms in figure 2, and lines—global fit of the real and imaginary conductivity to the Drude-Smith model (solid red line—fit to σ_1, dashed blue line—fit to σ_1). (b) Drude-Smith fits to σ_1 and σ_2 without excitation (as shown in (a)) and 3 ps following excitation with ~280 μJ cm^{-2}, 800 nm pulse. (c) Change in complex THz conductivity at different times after excitation.

phase of the THz pulses transmitted through the sample on a substrate and through the substrate alone using a relation $\frac{\tilde{E}_{sample}(\omega)}{\tilde{E}_{substrate}(\omega)} = \frac{n+1}{n+1+Z_0\tilde{\sigma}(\omega)}$, where $Z_0 = 377\Omega$ is the impedance of the free space, and n is the substrate refractive index in THz range [25]. For glass, $n \approx 1.96$ and can be treated as dispersionless in the frequency range of interest [33].

Resulting complex sheet conductivity spectrum is shown in figure 3(a). The periodic modulation seen at low frequencies is an artefact due to Fabry–Pérot interference of the THz probe pulse within the substrate, and we disregard it here. Complex sheet conductivity exhibits suppression of the real conductivity at low frequencies and negative imaginary conductivity. These features are characteristic of a system where free carriers motion on the mesoscopic length scales is constrained by potential barriers, such as often seen in nanocrystalline or granular systems [27, 34, 35]. Conductivity in such systems can be well-described by a classical Drude-Smith model, a modification of the free carrier Drude conductivity that accounts for localization of the mobile carriers on the length scales commensurate with their mean free path [27, 31, 34, 36–42].

In the Drude-Smith formalism, complex frequency-resolved conductivity is given as $\tilde{\sigma}(\omega) = \frac{\sigma_{DC}}{1-i\omega\tau_{DS}}\left(1+\frac{c}{1-i\omega\tau_{DS}}\right)$. Here, $\sigma_{DC} = \sigma(0) = \frac{Ne^2\tau_{DS}}{m^*}$ is Drude weight, or the conductivity in DC limit, τ_{DS} is a phenomenological carrier scattering time which takes into account both the bulk scattering τ_{bulk} and characteristic time associated with grain boundary scattering $\tau_{boundary}$ as $\frac{1}{\tau_{DS}} = \frac{1}{\tau_{bulk}} + \frac{1}{\tau_{boundary}}$, N is the charge carrier density, and m^* is the carrier effective mass. Phenomenological c-parameter is a measure of carrier localization over the probed length scales. When $c = 0$, the system is fully percolated and carriers free to move throughout the sample, as described by the Drude model. For $c = -1$, DC conductivity is suppressed as the carriers are localized over short distances. In figure 3(a), solid red symbols depict experimentally determined real conductivity, and open blue symbols—imaginary conductivity. Nearly dispersionless real conductivity at frequencies <1.7 THz and a negative imaginary conductivity indicates a free carrier system with a short scattering time and localization over mesoscopic length scales due to the presence of the nanoplatelet boudaries and/or defects that impede free carrier motion within the film. It should be noted that such complex conductivity spectra cannot be well-reproduced by the Lorentz conductivity model used to describe plasmon- and phonon-related effects, as frequency-dependent negative imaginary conductivity in the Lorentz model is accompanied by a significant dispersion in the real conductivity component [32]. Lines in figure 3(a) represent a global fit of real and imaginary conductivity to the Drude-Smith model with $\tau_{DS} = 6 \pm 1$ fs, and $c = -0.97 \pm 0.03$. Drude-Smith c-parameter that is close to -1 indicates that long-range conductivity in the film is strongly suppressed. However, even given this significant suppression of long-range transport, overall conductivity of the film is very high and extrapolates to ~300 $(\Omega\,\text{cm})^{-1}$ at $\omega = 0$ due to a very large, ~2×10^{21} cm^{-3} carrier density, calculated from the Drude-Smith fit to the THz conductivity using zone-center electron effective mass of 0.2845m_e [43]. Intrinsic carrier density determined from THz measurements is in reasonable agreement with the value determined from electrical measurements on individual nanoplatelets, $8 \pm 3 \times 10^{21}$ cm^{-3} [44]. Underestimation of carrier density in THz measurements results from averaging

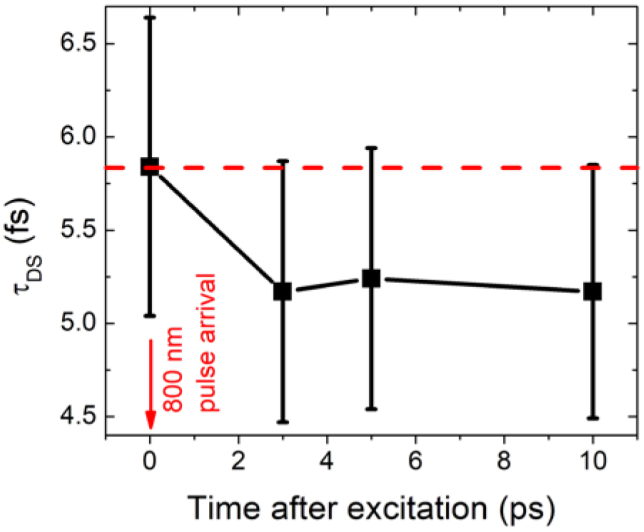

Figure 4. Change in the carrier scattering rate as a function of time following photoexcitation with ~280 μJ cm^{-2}, 800 nm pulse.

over a large, ~1.5 mm in diameter, area of the film that does not completely cover the surface (figure 1(c)). We calculate intrinsic carrier mobility, or mobility of carriers over mesoscopic length scales within individual grains to be $\mu_{intrinsic} = \frac{e\tau_{DS}}{m^*} \approx 34 \text{cm}^2\ \text{V}^{-1}\ \text{s}^{-1}$. However, the long range mobility in this film is strongly suppressed, and can be estimated from the intrinsic mobility as $\mu_{long\ range} = \mu_{intrinsic}(1+c)$. This calculation yields $\mu_{long\ range} \approx 1\ \text{cm}^2\ \text{V}^{-1}\ \text{s}^{-1}$. It is in agreement with the room temperature mobility within a single nanosheet of $0.7 \pm 0.2\,\text{cm}^2\ \text{V}^{-1}\ \text{s}^{-1}$ determined from electrical measurements [44] and supports our hypothesis that the free carrier motion is mainly impeded by the grain boundaries between different nanoplatelets within the thin film.

3.2. Optical pump—THz probe spectroscopy: non-equilibrium carrier dynamics

Many proposed application for the Mxenes involve their optical excitation. We studied the effects of photoexcitation with ~100 fs, 800 nm pulses on THz conductivity of the film. Linear optical absorbance of the film at 800 nm is ~15% based on UV–VIS measurements (figure 1(d)) [7]. At optical fluence of 280 μJ cm^{-2}, the absorbed photon flux is 17×10^{13} cm^{-2}. Resulting changes in the THz pulse transmission at a given fixed time delay between the optical pump and THz probe were detected by modulating the optical pump beam using a chopper and recording the differential electric field ΔE. The change in transmission of the THz probe pulse 3 ps after photoexcitation with ~280 μJ cm^{-2} pulse compared to the transmission through the unpumped film are shown as a blue curve in figure 2, multiplied by 100 for clarity. While the change is small (<0.3%), it is clear that photoexcitation enhances THz transmission, as the amplitude of the THz probe pulse transmitted through the photoexcited sample is higher compared to the amplitude of the THz probe pulse transmitted through the unexcited sample. Photoinduced transient changes in complex THz conductivity are summarized in figures 3(b) and (c). For a small differential change in transmission, complex differential change conductivity at a fixed pump-probe delay time was calculated as $\Delta\sigma(\omega) \approx -\frac{n+1}{Z_0}\frac{\Delta E(\omega)}{E(\omega)}$, where $E(\omega)$ is the electric field of the THz pulse transmitted through the unexcited film. Examples of the differential conductivity at 3 ps, 5 ps, and 10 ps after excitation with ~280 μJ cm^{-2} pulse are shown in 3(c). Transient real photoconductivity is negative at all these three time points, and in the entire sampled frequency range, demonstrating that photoexcitation suppresses conductivity of the film. This behavior is characteristic of metallic rather than semiconducting systems, and has been observed in graphene, thin metallic films and metallic RuO_2 [37, 40, 41, 45–50].

We analyze the temporal evolution of the complex conductivity following photoexcitation by fitting transient real ($\sigma_1(t) = \sigma_1 + \Delta\sigma_1(t)$) and imaginary ($\sigma_2(t) = \sigma_2 + \Delta\sigma_2(t)$) components to the Drude-Smith model. Lines in figure 3(b) represent the best fit to $\sigma_1(t)$ and $\sigma_2(t)$ at 3 ps following photoexcitation along with the best fit to THz conductivity in the unexcited film (figure 3(a)). Like the intrinsic conductivity of unexcited sample described above, conductivity of the photoexcited sample is well-described by the Drude-Smith model with unchanged c-parameter $c = -0.97 \pm 0.03$, indicating that photoexcitation does not affect localization of free carriers within the nanoplatelets. The observed change in carrier density is minimal, and cannot be reliably determined within the error of our measurement. Intraband photoexcitation of metallic materials does not result in a free carrier density increase, but rather increases carrier scattering due to lattice heating as hot carriers couple to phonon modes [40]. The carrier scattering time τ_{DS}, determined from global fits of the real and imaginary THz conductivity to the Drude-Smith model is

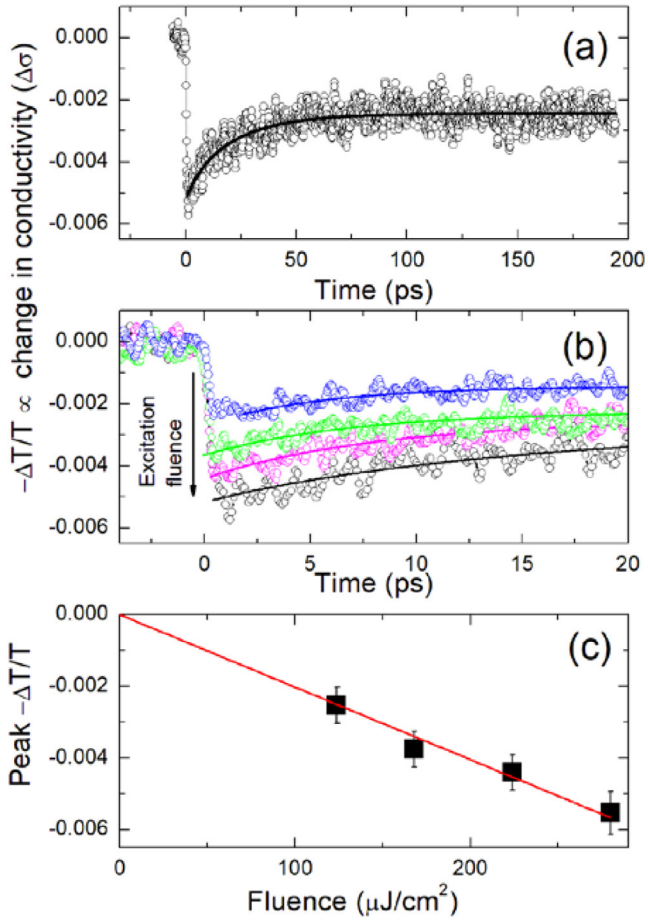

Figure 5. (a) Photoinduced change in the THz peak transmission as a function of time after photoexcitation with 280 μJ cm^{-2}, 800 nm pulse. Solid line shows the fit of THz transmission enhancement to a double-exponential decay. (b) Expanded view of transient peak THz transmission at different excitation fluence values from 120 μJ cm^{-2} to 280 μJ cm^{-2}, and (c) the corresponding peak THz transmission change as a function of excitation fluence.

shown in figure 4. Indeed, we find that the scattering time in the investigated time range 3–10 ps after optical excitation shows small but discernable decrease (figure 4), suggesting that increased carrier scattering in the major reason behind conductivity suppression. Improving the precision of both carrier density and the scattering rate would require THz measurements in the significantly broader spectral range.

The dynamics of the observed conductivity suppression are examined in figure 5. By monitoring the transient change in the transmission of the THz pulse peak as a function of the pump-probe delay time, we have characterized the duration of the observed conductivity suppression. Instrument-limited rise time of conductivity suppression is followed by the long, slow decay that persists for 200 ps and possibly beyond, to the time scale not accessible in our experiments. Figure 5(a) shows transient enhancement of THz peak transmission following photoexcitation with ~280 μJ cm^{-2} pulse. It can be fit to a bi-exponential decay (red solid line) with the fast component ~7 ± 1 ps, a slower component ~22 ± 2 ps, and a nearly constant offset that represents the long-lived component that we cannot reliably extract. This long decay of photoinduced conductivity suppression is similar to that observed in metallic (gold and chromium) thin films, and is significantly longer than in photoexcited graphene that shows a recovery within only a few picoseconds [37, 41, 46–51]. Decreasing excitation fluence to ~120 μJ cm^{-2} linearly reduces the amplitude of the observed response but does not change the dynamics in the studied range of excitation fluence (figures 5(b) and (c)). In metallic materials with static density of free carriers, photoexcitation does not significantly increase free carrier density. Strong electron–phonon coupling facilitates rapid, over the sub-picosecond time scales, equilibration of hot free carrier population with the lattice, resulting in a transient increase of lattice temperature. Carrier scattering is increased at elevated lattice temperatures, and recovery of background conductivity over time scales of hundreds of picoseconds represents lattice cooling as heat is transferred to the substrate and laterally—to the unexcited portions of the film.

4. Conclusion

We have investigated equilibrium and non-equilibrium dynamics of charge carriers in $Ti_3C_2T_x$ nanoplatelets. We find that the nanoplatelets are metallic, with a high (~2×10^{21} cm^{-3}) intrinsic charge carrier density and relatively high (~34 cm^2 V^{-1} s^{-1}) mobility of

carriers within individual nanoplatelets. High carrier density gives rise to exceptionally large, ~46 000 cm^{-1} absorption in the THz range, putting $Ti_3C_2T_x$ forth as a potential THz detector material alongside other 2D materials such as graphene and black phosphorus [52–54]. Photoexcitation results in a transient reduction of conductivity, as hot carriers rapidly heat the lattice, and the elevated lattice temperature enhances carrier scattering. As the lattice cools over the time scales of hundreds of picoseconds by transferring heat to the substrate and to the unexcited portions of the film, conductivity of $Ti_3C_2T_x$ nanoplatelet film recovers. The possibility to suppress conductivity and enhance THz transmission in $Ti_3C_2T_x$ by photoexcitation makes this new 2D material an attractive candidate for THz modulation devices and variable electromagnetic shielding applications.

Acknowledgments

The authors are deeply thankful to Dr D Turchinovich at University of Duisburg-Essen and Dr Yury Gogotsi at Drexel University for helpful discussions.

ORCID iDs

Vadym N Mochalin https://orcid.org/0000-0001-7403-1043
Lyubov V Titova https://orcid.org/0000-0002-2146-9102

References

[1] Anand B, Podila R, Lingam K, Krishnan S R, Siva Sankara Sai S, Philip R and Rao A M 2013 Optical diode action from axially asymmetric nonlinearity in an all-carbon solid-state device *Nano Lett.* **13** 5771–6
[2] Woodward R I, Howe R C T, Hu G, Torrisi F, Zhang M, Hasan T and Kelleher E J R 2015 Few-layer MoS_2 saturable absorbers for short-pulse laser technology: current status and future perspectives [Invited] *Photonics Res.* **3** A30–42
[3] Wang S, Yu H, Zhang H, Wang A, Zhao M, Chen Y, Mei L and Wang J 2014 Broadband few-layer MoS_2 saturable absorbers *Adv. Mater.* **26** 3538–44
[4] Lingam K, Podila R, Qian H, Serkiz S and Rao A M 2013 Evidence for edge-state photoluminescence in graphene quantum dots *Adv. Funct. Mater.* **23** 5062–5
[5] Wang Z, Mu H, Yuan J, Zhao C, Bao Q and Zhang H 2017 Graphene-Bi_2Te_3 heterostructure as broadband saturable absorber for ultra-short pulse generation in Er-doped and Yb-doped fiber lasers *IEEE J. Sel. Top. Quantum Electron.* **23** 195–9
[6] Yuan S, Roldán R, Katsnelson M I and Guinea F 2014 Effect of point defects on the optical and transport properties of MoS_2 and WS_2 *Phys. Rev.* B **90** 041402
[7] Dong Y, Chertopalov S, Maleski K, Anasori B, Hu L, Bhattacharya S, Rao A M, Gogotsi Y, Mochalin V N and Podila R 2018 Saturable absorption in 2D Ti_3C_2 MXene thin films for passive photonic diodes *Adv. Mater.* **30** 1705714
[8] Nair R R, Blake P, Grigorenko A N, Novoselov K S, Booth T J, Stauber T, Peres N M R and Geim A K 2008 Fine structure constant defines visual transparency of graphene *Science* **320** 1308–8
[9] Butler S Z *et al* 2013 Progress, challenges, and opportunities in two-dimensional materials beyond graphene *ACS Nano* **7** 2898–26
[10] Jhon Y I, Koo J, Anasori B, Seo M, Lee J H, Gogotsi Y and Jhon Y M 2017 Metallic MXene saturable absorber for femtosecond mode-locked lasers *Adv. Mater.* **29** 1702496
[11] Jiang X *et al* 2018 Broadband nonlinear photonics in few-layer MXene $Ti_3C_2T_x$ (T = F, O, or OH) *Laser Photonics Rev.* **12** 1700229
[12] Naguib M, Mochalin V N, Barsoum M W and Gogotsi Y 2014 25th anniversary article: MXenes: a new family of two-dimensional materials *Adv. Mater.* **26** 992–1005
[13] Anasori B, Lukatskaya M R and Gogotsi Y 2017 2D metal carbides and nitrides (MXenes) for energy storage *Nat. Rev. Mater.* **2** 16098
[14] Dillon A D, Ghidiu M J, Krick A L, Griggs J, May S J, Gogotsi Y, Barsoum M W and Fafarman A T 2016 Highly conductive optical quality solution-processed films of 2D titanium carbide *Adv. Funct. Mater.* **26** 4162–8
[15] Zhang C, Anasori B, Seral-Ascaso A, Park S H, McEvoy N, Shmeliov A, Duesberg G S, Coleman J N, Gogotsi Y and Nicolosi V 2017 Transparent, flexible, and conductive 2D titanium carbide (MXene) films with high volumetric capacitance *Adv. Mater.* **29** 1702678
[16] Lipatov A, Alhabeb M, Lukatskaya M R, Boson A, Gogotsi Y and Sinitskii A 2016 Effect of synthesis on quality, electronic properties and environmental stability of individual monolayer Ti_3C_2 MXene flakes *Adv. Electron. Mater.* **2** 1600255
[17] Shahzad F, Alhabeb M, Hatter C B, Anasori B, Man Hong S, Koo C M and Gogotsi Y 2016 Electromagnetic interference shielding with 2D transition metal carbides (MXenes) *Science* **353** 1137–40
[18] Xiao B, Li Y-C, Yu X-F and Cheng J-B 2016 MXenes: reusable materials for NH_3 sensor or capturer by controlling the charge injection *Sensors Actuators* B **235** 103–9
[19] Tan T L, Jin H M, Sullivan M B, Anasori B and Gogotsi Y 2017 High-throughput survey of ordering configurations in MXene alloys across compositions and temperatures *ACS Nano* **11** 4407–18
[20] Dong Y, Mallineni S S K, Maleski K, Behlow H, Mochalin V N, Rao A M, Gogotsi Y and Podila R 2018 Metallic MXenes: a new family of materials for flexible triboelectric nanogenerators *Nano Energy* **44** 103–10
[21] Dai C, Chen Y, Jing X, Xiang L, Yang D, Lin H, Liu Z, Han X and Wu R 2017 Two-dimensional tantalum carbide (MXenes) composite nanosheets for multiple imaging-guided photothermal tumor ablation *ACS Nano* **11** 12696–712
[22] Feng W, Luo H, Wang Y, Zeng S, Deng L, Zhou X, Zhang H and Peng S 2018 Ti_3C_2 MXene: a promising microwave absorbing material *RSC Adv.* **8** 2398–403
[23] Choi G *et al* 2018 Enhanced terahertz shielding of MXenes with nano-metamaterials *Adv. Opt. Mater.* **6** 1701076
[24] Jhon Y I, Seo M and Jhon Y M 2018 First-principles study of a MXene terahertz detector *Nanoscale* **10** 69–75
[25] Jepsen P U, Cooke D G and Koch M 2011 Terahertz spectroscopy and imaging–Modern techniques and applications *Laser Photonics Rev.* **5** 124–66
[26] Baxter J B and Guglietta G W 2011 Terahertz spectroscopy *Anal. Chem.* **83** 4342–68
[27] Cocker T L, Titova L V, Fourmaux S, Bandulet H C, Brassard D, Kieffer J C, El Khakani M A and Hegmann F A 2010 Terahertz conductivity of the metal-insulator transition in a nanogranular VO_2 film *Appl. Phys. Lett.* **97** 221905
[28] Baxter J B and Schmuttenmaer C A 2009 Carrier dynamics in bulk ZnO. I. Intrinsic conductivity measured by terahertz time-domain spectroscopy *Phys. Rev.* B **80** 235206
[29] Ulbricht R, Hendry E, Shan J, Heinz T F and Bonn M 2011 Carrier dynamics in semiconductors studied with time-resolved terahertz spectroscopy *Rev. Mod. Phys.* **83** 543–86
[30] Butler K T, Dringoli B J, Zhou L, Rao P M, Walsh A and Titova L V 2016 Ultrafast carrier dynamics in $BiVO_4$ thin film photoanode material: interplay between free carriers, trapped carriers and low-frequency lattice vibrations *J. Mater. Chem.* A **4** 18516–23

[31] Titova L V, Cocker T L, Xu S, Baribeau J-M, Wu X, Lockwood D J and Hegmann F A 2016 Ultrafast carrier dynamics and the role of grain boundaries in polycrystalline silicon thin films grown by molecular beam epitaxy *Semicond. Sci. Technol.* **31** 105017
[32] Lloyd-Hughes J and Jeon T-I 2012 A review of the terahertz conductivity of bulk and nano-materials *J. Infrared Millim. Terahertz Waves* **33** 871–925
[33] Naftaly M and Miles R E 2007 Terahertz time-domain spectroscopy for material characterization *Proc. IEEE* **95** 1658–65
[34] Titova L V, Cocker T L, Cooke D G, Wang X, Meldrum A and Hegmann F A 2011 Ultrafast percolative transport dynamics in silicon nanocrystal films *Phys. Rev.* B **83** 085403
[35] Baxter J B and Schmuttenmaer C A 2006 Conductivity of ZnO nanowires, nanoparticles, and thin films using time-resolved terahertz spectroscopy *J. Phys. Chem.* B **110** 25229–39
[36] Cocker T L, Baillie D, Buruma M, Titova L V, Sydora R D, Marsiglio F and Hegmann F A 2017 Microscopic origin of the Drude-Smith model *Phys. Rev.* B **96** 205439
[37] Jensen S A, Ulbricht R, Narita A, Feng X, Mullen K, Hertel T, Turchinovich D and Bonn M 2013 Ultrafast photoconductivity of graphene nanoribbons and carbon nanotubes *Nano Lett.* **13** 5925–30
[38] Guglietta G W, Diroll B T, Gaulding E A, Fordham J L, Li S, Murray C B and Baxter J B 2015 Lifetime, mobility, and diffusion of photoexcited carriers in ligand-exchanged lead selenide nanocrystal films measured by time-resolved terahertz spectroscopy *ACS Nano* **9** 1820–8
[39] Richter C and Schmuttenmaer C A 2010 Exciton-like trap states limit electron mobility in TiO_2 nanotubes *Nat. Nanotechnol.* **5** 769
[40] Alberding B G, DeSario P A, So C R, Dunkelberger A D, Rolison D R, Owrutsky J C and Heilweil E J 2017 Static and time-resolved terahertz measurements of photoconductivity in solution-deposited ruthenium dioxide nanofilms *J. Phys. Chem.* C **121** 4037–44
[41] Alberding B G, Kushto G P, Lane P A and Heilweil E J 2016 Reduced photoconductivity observed by time-resolved terahertz spectroscopy in metal nanofilms with and without adhesion layers *Appl. Phys. Lett.* **108** 223104
[42] Walther M, Cooke D G, Sherstan C, Hajar M, Freeman M R and Hegmann F A 2007 Terahertz conductivity of thin gold films at the metal-insulator percolation transition *Phys. Rev.* B **76** 125408
[43] Hu T, Zhang H, Wang J, Li Z, Hu M, Tan J, Hou P, Li F and Wang X 2015 Anisotropic electronic conduction in stacked two-dimensional titanium carbide *Sci. Rep.* **5** 16329
[44] Miranda A, Halim J, Barsoum M W and Lorke A 2016 Electronic properties of freestanding $Ti_3C_2T_x$ MXene monolayers *Appl. Phys. Lett.* **108** 033102
[45] Tielrooij K J, Massicotte M, Piatkowski L, Woessner A, Ma Q, Jarillo-Herrero P, van Hulst N F and Koppens F H L 2015 Hot-carrier photocurrent effects at graphene–metal interfaces *J. Phys.: Condens. Matter* **27** 164207
[46] Jnawali G, Rao Y, Yan H and Heinz T F 2013 Observation of a transient decrease in terahertz conductivity of single-layer graphene induced by ultrafast optical excitation *Nano Lett.* **13** 524–30
[47] Frenzel A J, Lui C H, Fang W, Nair N L, Herring P K, Jarillo-Herrero P, Kong J and Gedik N 2013 Observation of suppressed terahertz absorption in photoexcited graphene *Appl. Phys. Lett.* **102** 113111
[48] Docherty C J, Lin C-T, Joyce H J, Nicholas R J, Herz L M, Li L-J and Johnston M B 2012 Extreme sensitivity of graphene photoconductivity to environmental gases *Nat. Commun.* **3** 1228
[49] Ivanov I, Bonn M, Mics Z and Turchinovich D 2015 Perspective on terahertz spectroscopy of graphene *Europhys. Lett.* **111** 67001
[50] Tomadin A *et al* 2018 The ultrafast dynamics and conductivity of photoexcited graphene at different Fermi energies *Sci. Adv.* **4**
[51] Anand B, Karakaya M, Prakash G, Sankara Sai S S, Philip R, Ayala P, Srivastava A, Sood A K, Rao A M and Podila R 2015 Dopant-configuration controlled carrier scattering in graphene *RSC Adv.* **5** 59556–63
[52] Leonardo V, Jin H, Dominique C, Wojciech K, Alessandro T, Antonio P and Serena V M 2015 Black phosphorus terahertz photodetectors *Adv. Mater.* **27** 5567–72
[53] Leong E, Suess R J, Sushkov A B, Drew H D, Murphy T E and Mittendorff M 2017 Terahertz photoresponse of black phosphorus *Opt. Express* **25** 12666–74
[54] Koppens F H L, Mueller T, Avouris P, Ferrari A C, Vitiello M S and Polini M 2014 Photodetectors based on graphene, other two-dimensional materials and hybrid systems *Nat. Nanotechnol.* **9** 780